Synthesis, characterization, and evaluation of polyaniline-modified $(FeCoNiCrMn)_3O_4$ high-entropy oxide as an anode material for lithium-ion batteries

Jari, Arezoo; Panjepour, Masoud; Bahrami, Abbas; Yazdan Mehr, Maryam

DOI
10.1016/j.matchemphys.2024.130322

Publication date
2025

Document Version
Final published version

Published in
Materials Chemistry and Physics

Materials Chemistry and Physics 333 (2025) 130322

Contents lists available at ScienceDirect

Materials Chemistry and Physics

journal homepage: www.elsevier.com/locate/matchemphys

Synthesis, characterization, and evaluation of polyaniline-modified $(FeCoNiCrMn)_3O_4$ high-entropy oxide as an anode material for lithium-ion batteries

Arezoo Jari [a], Masoud Panjepour [a], Abbas Bahrami [a,*], Maryam Yazdan Mehr [b]

[a] Department of Materials Engineering, Isfahan University of Technology, Isfahan 84156-83111, Iran
[b] Faculty EEMCS, Delft University of Technology, Mekelweg 4, 2628 CD Delft, The Netherlands

HIGHLIGHTS

- The microstructure and electrochemical properties of Polyaniline (PANI)-Modified $(FeCoNiCrMn)_3O_4$ have been investigated.
- The PANI coating significantly improves the reactions between electrodes and electrolyte.
- The PANI-modified powder samples showed promising properties as anodes in Li-ion batteries.
- The correlations between the microstructure and electrochemical properties of samples have been investigated.

ARTICLE INFO

Keywords:
High-entropy oxide
Polyaniline
Lithium ion battery
Anode

ABSTRACT

This paper investigates the microstructure and electrochemical properties of Polyaniline-Modified $(FeCoNiCrMn)_3O_4$, a high-entropy oxide, with a focus on its potential as an anode material in lithium-ion batteries. The high-entropy oxide $(FeCoNiCrMn)_3O_4$, featuring a spinel structure, was synthesized via a two-step process: mechanical milling of constituent oxides followed by a calcination treatment at 900 °C. To investigate the structure of the synthesized powder, scanning electron microscope (SEM), energy-dispersive X-ray spectroscopy (EDS), and X-ray diffraction (XRD) were employed. The results demonstrate the successful synthesis of a single-phase spinel structure with a homogeneous distribution of elements, exhibiting perfect uniformity. A Polyaniline (PANI) coating layer was subsequently applied to the HEO particles using a polymerization method. The presence of the PANI layer was confirmed using Fourier Transform Infrared Spectroscopy (FTIR). Results from impedance analysis revealed a substantial decrease in the Z-value of the PANI-modified sample compared to the pure HEO, indicating that the modified anode exhibits enhanced electrical conductivity. It is evident that the PANI coating layer has a significantly positive attribution to the electrochemical performance of the anode material by enhancing its structural stability and inhibiting excessive solid electrolyte interphase (SEI) growth during cycling. The correlations between the HEO structure and the PANI layer with the electrochemical performance of the anode material are discussed.

1. Introduction

The growing demand for high power/high energy density lithium-ion batteries is driven by the increasing adoption of advanced electronics and electric vehicles [1–4]. Extensive research efforts have focused on developing electrode materials that can deliver high reversible specific capacities, rapid charging and discharging rates, and long cycle life [4–6]. Graphite is the preferred anode material in commercial Li-ion batteries due to its low cost, low operating voltage, and reliable cycling performance, but its theoretical capacity (372 mA h g^{-1}) and resistance to lithium-ion transfer limit its overall performance [7,8]. To address these challenges, research has shifted towards alternative complex anode materials, including alloys and conversion anodes. These materials deliver high capacities due to their ability to undergo advanced multi-electron redox mechanisms, offering several advantages over graphite, including improved performance and safer

* Corresponding author.
E-mail address: a.n.bahrami@iut.ac.ir (A. Bahrami).

https://doi.org/10.1016/j.matchemphys.2024.130322
Received 1 October 2024; Received in revised form 20 December 2024; Accepted 20 December 2024
Available online 24 December 2024

operating voltages [9–14]. However, most of alternative anode materials are susceptible to significant volume changes and pulverization during lithiation and de-lithiation cycles, which can cause mechanical damage to electrical connections, compromise the stability of the solid electrolyte interphase (SEI), and result in rapid capacity degradation [15,16]. Despite this challenge, it is crucial to develop innovative electrode materials that balance high storage capacity, structural integrity, and electrical conductivity. This balance is key to future advancements in the battery industry. Among these alternative materials, high-entropy oxides (HEOs) stand out due to their unique structural and electrochemical properties, making them a promising candidate for enhancing Li-ion battery performance.

High-entropy materials, including oxides, carbides, and nitrides, are a relatively recent development in materials design, characterized by mixing alloying components in equi-molar ratios [17–19]. High-entropy oxides (HEOs) have attracted significant attention due to their unique properties. However, challenges remain in understanding their behavior under cycling conditions and optimizing their performance for practical applications. This study seeks to investigate the impact of PANI modification on these properties, with the goal of improving both performance and longevity in Li-ion batteries [20]. The first reported HEOs was a rock-salt oxide with the composition $(Mg_{0.2}Co_{0.2}Ni_{0.2}Cu_{0.2}Zn_{0.2})O$, which exhibited exceptional structural stability due to its high entropy [21]. Subsequent research, including a study by Breitung et al., has demonstrated that HEOs may play a role in energy storage systems [22]. Tian et al. recently demonstrated that the use of high-entropy design in layered oxides can effectively suppress phase transitions and enhance the cycling stability of sodium-ion batteries by stabilizing the layered structure and enabling reversible electrochemical reactions [23]. Moreover, the HEO anodes have shown significantly improved cycling stability compared to conversion-type anode materials, owing to the high entropy stabilization effects of HEO [24]. As a newly developed category of single-phase materials, HEOs exhibit promising properties that are still being explored [25,26]. Recently, the focus has shifted to high entropy spinel oxides, which share similarities with other HEO structures [27–29]. Nguyen et al. [30] and Wang et al. [31] synthesized an equimolar $(FeCoNiCrMn)_3O_4$ HEO with a spinel structure, which exhibited enhanced 3D pathways for lithium-ion diffusion. This structure, unlike rock-salt, has two distinct Wyckoff sites available for trivalent ions, leading to a broader valence range during charging and discharging. This, in turn, enables an increased capacity for anode materials. Furthermore, the elements within the $(FeCoNiCrMn)_3O_4$ oxide structure have similar atomic radii and exhibit significant solubility in both binary and ternary subsystems, contributing positively to the structural stability of HEO. However, there is still scope for the improvement in electrical conductivity and structural stability, which can enhance rate performance and cycling stability respectively [32–34].

In Li-ion batteries, smaller active material particles enhance lithium-ion diffusion and increase the interfacial area, improving lithium-ion migration between the material and the electrolyte. Nevertheless, it is noteworthy that a very large specific surface areas of nanoparticles can in some cases cause particle agglomeration and irreversible reactions. Consequently, materials are often coated with stable compounds such as oxides, carbons, and polymers to control interface reactions [35–37]. Currently, researchers are focusing on the development of anode materials blended with conducting polymers to enhance battery performance. Among the various conducting polymers, polyaniline (PANI) has garnered significant attention due to its exceptional electrical conductivity, superior structural stability, and ease of synthesis. The PANI coating is expected to enhance both the electrical conductivity and structural integrity of the HEO material, addressing key challenges such as volume expansion during cycling and stability of the SEI [38–40].

This study focuses on improving the electrochemical performance of $(FeCoNiCrMn)_3O_4$-type HEO anodes by coating them with polyaniline (PANI), aiming to enhance their conductivity and structural stability for use in Li-ion batteries. The modified HEO particles will be coated with a PANI layer on their external surface to enhance their overall surface characteristics. The effects of PANI surface modification on the conductivity and structural stability of the HEO particles have been investigated. By addressing these key challenges, this study aims to develop a novel PANI-coated HEO anode material with enhanced electrochemical properties, offering a potential solution for next-generation Li-ion batteries.

2. Experimental

2.1. Synthesis of HEO and PANI-modified HEO samples

Equimolar amounts of the oxides, Fe_2O_3, Co_3O_4, NiO, Cr_2O_3 and MnO_2 (all sourced from Merck) were mixed using a planetary ball mill for 2, 4, and 6 h at a rotating speed of 300 rpm. Then, the oxide powders were then heated to 900 °C for 12 h in a tube furnace, followed by natural cooling to room temperature. The following procedure was used to synthesize PANI-modified HEO samples (HEO-P). First, 0.5 g of HEO was mixed with 50 mL of deionized water using ultrasound for 30 min. Next, 0.15 mL of aniline monomer and 0.3 mL of a 50 % phytic acid solution were added, and the mixture was stirred for 12 h. Subsequently, a solution of 0.2 g of ammonium persulfate (APS) was added to the mixture. After reacting 4 h, the resulting product was collected by centrifuging and washed several times with deionized water and ethanol. The final powder was dried in a vacuum oven at 50 °C for 24 h. As a reference sample, pure PANI was also synthesized using the same process, except without HEO.

2.2. Materials characterization

The X-ray diffractometer (XRD, Philips using Cu Ka radiation) was used for phase identifications. Fourier-transformed infrared (FTIR, Bruker Tensor 27) analysis was conducted to gain insight into the formation of PANI coating on HEO particles. Chemical analysis of the synthesized powder particles was carried out using energy dispersive X-ray spectroscopy (EDS) with a Seron AIS 2300 system. The morphology of prepared samples was characterized by field emission scanning electron microscope (FE-SEM, FEI QUANTA FEG-450). Additionally, transmission electron microscope (TEM, JEOL JSM-6710F) was also used to further investigate the morphology and elemental mapping of synthesized HEO powders.

2.3. Electrochemical property measurements

Testing of electrochemical performance was done with CR2032 coin cells. The working electrodes, comprising HEO and HEO-PANI for lithium ion batteries, were fabricated by mixing active materials, carbon black (10 wt %) and polyvinylidene fluoride (PVDF) (10 wt %) with N-methyl pyrrolidone (NMP) as solvent to form a slurry with a weight ratio of 80:10:10. The slurry was then coated onto Cu foil, serving as the current collector, with a loading mass of 1.5 mg cm^{-2}. After coating, the electrodes were dried in a vacuum oven at 80 °C for 24 h. The half-cells were assembled in an Ar-filled glove box (SMART LINE, H_2O/O_2 content $<$0.1 ppm) using a 1 M solution of $LiPF_6$ in a 1:1:1 volumetric ratio of ethylene carbonate (EC), ethyl methyl carbonate (EMC), and dimethyl carbonate (DEC) as the electrolyte. The counter/reference electrode was a lithium disk (400 μm thick, sourced from Alfa Aesar), while a Celgard 2325 separator (25 μm thick, consisting of three layers of polypropylene/polyethylene/polypropylene) was used to separate the electrodes. The charge/discharge measurements were performed using a NEWARE battery testing system with a current capacity of 10 A and a voltage range of 5 V, operating within a voltage range of 0.01–3.0 V. Electrochemical impedance spectroscopy (EIS) was performed on an electrochemical workstation (SP50e Bio Logic) over a frequency range of 0.01 Hz–100 kHz.

3. Results and discussion

To synthesize $(FeCoNiCrMn)_3O_4$ HEO powders, equimolar amounts of Fe_2O_3, Co_3O_4, NiO, Cr_2O_3 and MnO_2 powders were mixed and subjected to mechanical activation through ball milling. This mixture was then calcined at 900 °C to facilitate the interdiffusion of the constituent elements and the formation of a homogeneous oxide solid solution. At high temperatures, the elements are expected to interdiffuse and replace each other at atomic sites, resulting in changes to the unit cell volume. These diffusion-based reactions finally lead to the formation of a single-phase metal oxide HEO structure. The calcined HEO particles were uniformly dispersed through ultrasonic vibration, followed by surface polymerization initiated by ammonium persulfate, which ultimately resulted in the formation of a PANI coating layer over particles, hereafter referred to as the HEO-P sample. The XRD patterns of the samples synthesized with varying milling times, both in their as-milled and heat-treated states at 900 °C, show different crystalline phases, as illustrated in Fig. 1. The starting compositions, comprising Fe_2O_3, Co_3O_4, NiO, Cr_2O_3 and MnO_2, are clearly visible in Fig. 1a. After 2 h of milling, the peaks corresponding to Fe_2O_3, Co_3O_4, NiO compositions have disappeared, whereas the dominant crystalline structure, the Fe_3O_4 spinel structure, start to form. Meanwhile, Cr_2O_3 and MnO_2 oxide appear to be relatively stable throughout the milling process. As shown in Fig. 1c, after 4 h of milling, there was little change in the phase compositions, with only two peaks, related to Cr_2O_3, fading. Finally, after 6 h of ball milling, MnO_2 peaks were disappeared, while Cr_2O_3 peaks remained present in the powder mixture, indicating that chromium oxide is one of the most stable oxides among the constituent oxides. The observed broadening of diffraction peaks with increasing milling time, as illustrated in Fig. 1b–d, is attributed to the gradual decrease in the crystallite size during mechanical milling. XRD results show that calcination at 900 °C results in the formation of a single cubic spinel phase structure of the Fd $\overline{3}$ m space group (COD No. 9005841). The high peak intensity and narrow peaks in the heat-treated sample indicate great crystallinity. The lattice parameter, calculated from the XRD pattern in Fig. 1e, is 8.344 Å, indicating a well-defined crystal structure. The spinel structure provides excellent three-dimensional channels for Li ion insertion and extraction, thereby enhancing the rate capability of anode materials. Notably, no peak attributable to impurities of any other kind of intermetallic compound was observed, suggesting the high purity of the final spinel composition. As shown in Fig. 1f, the crystalline structure of the final powder remains unchanged after coating with polyaniline, confirming that the PANI-modified high entropy oxide powder retains its spinel structure.

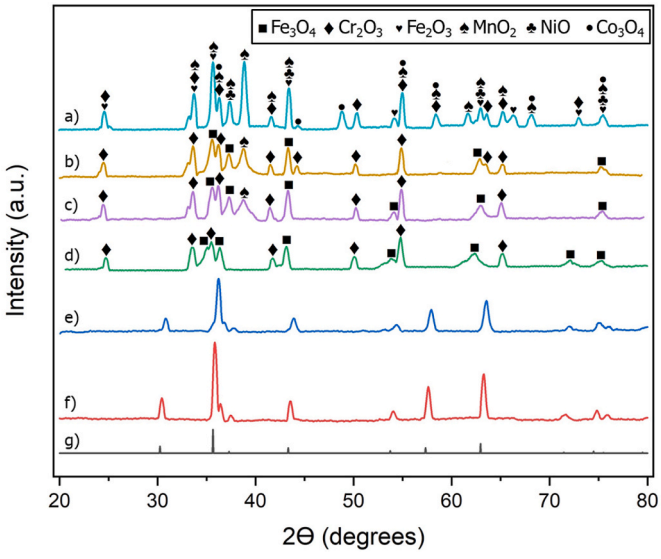

Fig. 1. X-Ray diffraction patterns of powder samples: a) before ball mill, b) after 2 h, c) 4 h, d) 6h of milling, and e) HEO particles after calcination, f) HEO-P particles, and g) the COD pattern with database (code 9005841).

A composition is typically considered to have high entropy when $S_{mix} \geq 1.5R$, where R represents the gas constant [41]. The configurational entropy was calculated using the following formula [42–46]:

$$\Delta S_{config} = -R\left[\left(\sum_{i=1}^{n} x_i \ln x_i\right)_{cation\text{-}site} + \left(\sum_{j=1}^{m} x_j \ln x_j\right)_{anion\text{-}site}\right] \quad (1)$$

where x_i represents the molar fraction of cations, using approximations for the molar fractions of the five cations. The molar fraction of anions is denoted by x_j, with the impact of individual anions on S_{conf} considered negligible and therefore disregarded. According to Eq. (1), the calculated value of S_{conf} is approximately 1.61R, suggesting that from an entropy perspective, this composition is a high-entropy oxide.

The presence of the PANI coating layer on the HEO surface was further investigated using FT-IR spectroscopy, as shown in Fig. 2. The FT-IR spectrum of pure PANI exhibits a distinct peak at 1577 cm^{-1}, which is attributed to N = Q = N stretching vibration. The 1500 cm^{-1} band corresponds to the C═C stretching vibration, while the peak at 1294 cm^{-1} is associated with the C–N stretching vibration of an aromatic amine. Additionally, the bands at 1093 cm^{-1} and 614 cm^{-1} are assigned to the in-plane and out-of-plane vibrations of C–H on the benzene ring, respectively. Also, the –OH stretching vibration at 3440 cm^{-1} may be attributed to adsorbed water molecules [47–49].

As expected, the characteristic peaks of PANI are evident in the HEO-P spectrum, implying that PANI has been successfully incorporated and combined with HEO particles. The porous structure of the PANI layer, coupled with its conductivity, is likely to significantly enhance the electrochemical performance of the anode material, which is expected to be beneficial for the overall device.

Fig. 3a represents the TEM image of HEO, which exhibits particle sizes ranging from approximately 2 μm after heat treatment. During the sintering process, the nano-sized HEO particles are aggregated and their crystallite size increases as a results of exposure to high temperatures. To mitigate the negative effects of this aggregation, the final powders were milled for a few minutes. Reduced nanoparticles aggregation during Li-ion electrodes fabrication results in more active sites for charge storage, leading to improved properties such as higher capacity, rate capability, and better reversibility. To further investigate the microstructure of HEO powders, HRTEM technique was employed. HRTEM image of HEO are depicted in Fig. 3b, which show lattice spacing of 0.480 and 0.289

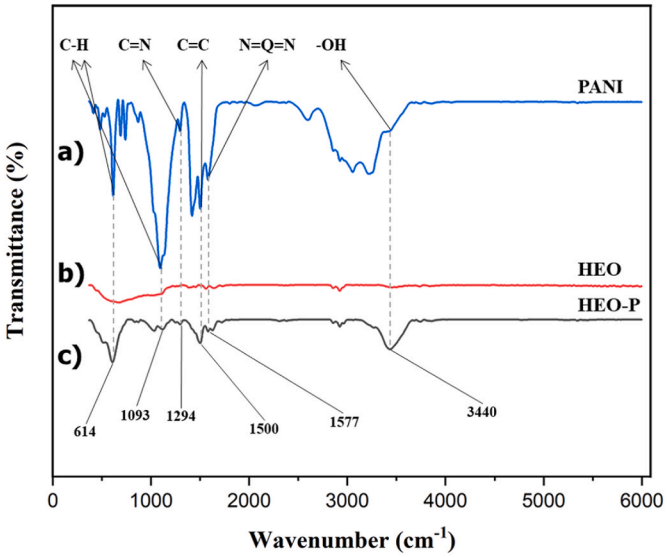

Fig. 2. FTIR spectra of a) PANI, b) HEO, and (c) HEO-P.

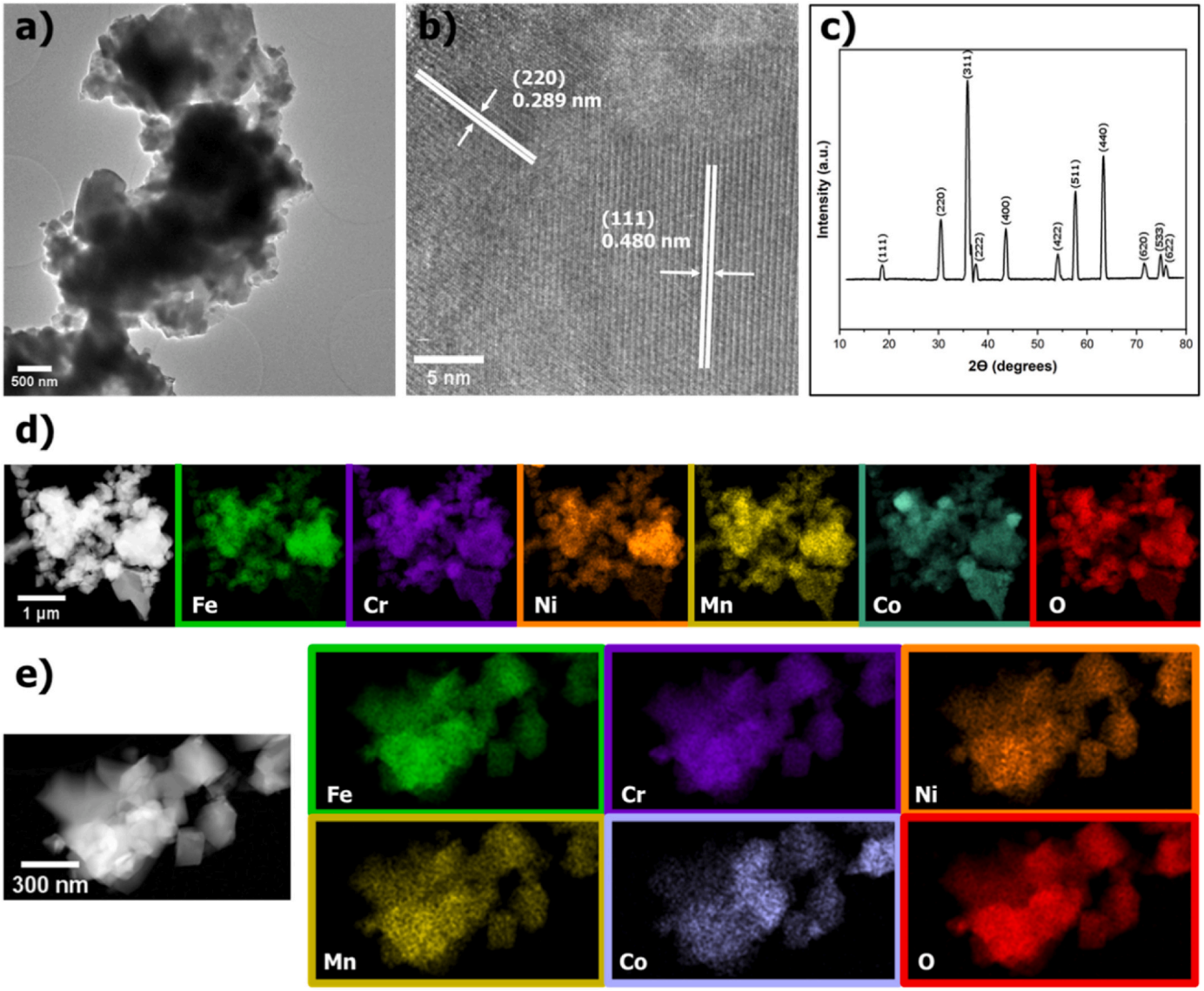

Fig. 3. a) TEM image, b) HRTEM image, c) XRD and d, e) elemental mapping images of the HEO particles.

nm corresponding to the (111) and (220) lattice planes in the spinel structure. In this regard, X-ray diffraction from 10° to 80° are presented in Fig. 3c. The diffraction peaks at 18.40°, 30.27°, 35.65°, 37.30°, 43.34°, 53.77°, 57.33°, 63°, 71.44°, 74.51°, and 75.52° can be indexed to the (1 1 1), (2 2 0), (3 1 1), (2 2 2), (4 0 0), (4 2 2), (5 1 1), (4 4 0), (6 2 0), (5 3 3) and (6 2 2) planes of the spinel structure HEO. Additionally, Fig. 3d, e shows TEM-EDS elemental mapping of HEO at two different magnifications, detecting signals of Fe, Cr, Ni, Co, and Mn elements. All of these elements are homogeneously distributed throughout the sample with no obvious indication of elemental segregation.

To further investigate the elemental composition of HEO-P powders, the EDS analyses and elemental mappings of HEO-P powders are compared to those of $(FeCoNiCrMn)_3O_4$ particles before and after ball milling (Fig. 4). The results show that the signals of Fe, Cr, Ni, Mn and Co elements are all well detected. As expected, initial powder mixture exhibits of different elements from various oxide precursors (Fig. 4a). After milling, the elements are homogeneously distributed throughout the powder, with no obvious signs of elemental segregation, thereby confirming aforementioned arguments on the uniform distribution of elements during milling.

However, the measured atomic percentages deviate from the theoretical nominal values. In the stoichiometric $(FeCoNiCrMn)_3O_4$ structure, the oxygen content contributes significantly to the total atomic composition, leaving the theoretical nominal atomic percentage of each metal cation at approximately 14.29 %. As shown in Table 1, the measured values, particularly for Co, appear significantly lower than this nominal value. This discrepancy is attributed to the inherent limitations of the EDS technique, such as detector sensitivity, spectral overlap, and surface measurement effects, which may affect the detection accuracy of certain elements. Additionally, differences in atomic weights of the constituent elements influence the measured weight percentages, further contributing to the observed deviations in atomic ratios.

While EDS provides valuable insights into elemental presence, it has limitations in accurately representing the true bulk composition. To confirm the uniformity of the elemental distribution, complementary techniques such as TEM mapping were employed, which provide higher resolution and sensitivity. TEM mapping results confirm that all elements, including Co and Ni, are homogeneously distributed throughout the HEO-P structure, supporting the material's structural homogeneity and suitability for electrochemical applications.

Additionally, the milling process is accompanied by a dramatic decrease in particle size, resulting in a uniform and even size distribution in the as-milled powder mixture. The presence of C and N peaks in

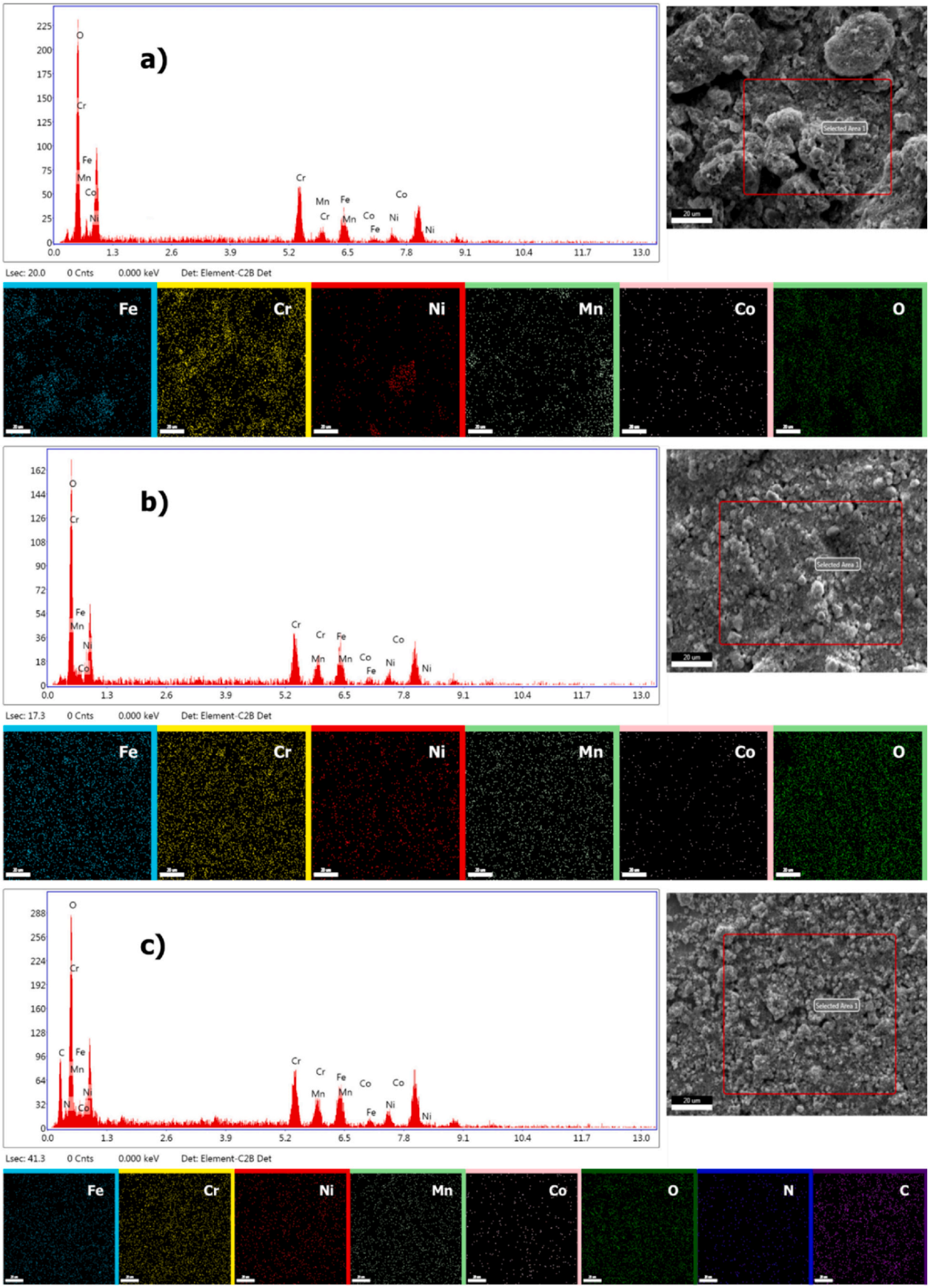

Fig. 4. EDS analysis and elemental mapping of the $(FeCoNiCrMn)_3O_4$ particles a) before, b) after ball mill, and c) HEO-P.

Table 1
Measured composition of elements in HEO-P from EDS analysis.

Element	Measured Weight %	Measured Atomic %
Fe	10.94	4.31
Cr	16.02	6.78
Ni	7.10	2.66
Mn	4.41	1.77
Co	0.18	0.07
O	61.34	84.40

the EDS of HEO-P sample, which are absent in pure HEO powder samples, again confirms that the fact that the surface of HEO particles is extensively covered with PANI in PANI-modified specimen.

To evaluate the electrochemical characteristics of the HEO-P and HEO electrodes, galvanostatic cycling was performed on coin cells constructed within a voltage range of 0.01–3.0 V vs. Li/Li^+. The electrochemical performance of the half-cells is illustrated in Fig. 5. Fig. 5a depicts a schematic of the half-cell, while Fig. 5b and c shows the initial galvanostatic charge–discharge curves of HEO and HEO-P at C-rates of C/10 ($1C = 2\ A\ g^{-1}$). In Fig. 5c, a potential plateau emerges around 1.0–0.5 V during discharging, transitioning to 1.5–2.0 V during charge, indicative of metal oxide reduction and SEI layer formation. Subsequently, a slope appears in place of a plateau from the second cycle, suggesting structural rearrangement and varying reaction voltages for different metals.

The initial discharge/charge specific capacities of HEO-P are 964 mA h g^{-1} and 612 mA h g^{-1}, respectively, with an initial coulombic efficiency (ICE) of 63.5 %. Following the initial cycle, the coulombic efficiency increased to around 90 % and remained stable throughout the testing period. The formation of the solid electrolyte interphase (SEI) film can be attributed to the irreversible capacity and low ICE in the first cycle. HEO exhibits lithiation and de-lithiation capacities of 827 and 445 mA h g^{-1}, respectively, corresponding to a first-cycle coulombic efficiency (CE) of 53.8 %. This highlights the improved capacity of HEO-P due to the PANI coating introduction.

The rate capability of the HEO and HEO-P anodes was evaluated at different C-rates, ranging from C/10 to 1C, as depicted in Fig. 5d. The corresponding galvanostatic curves are shown in Fig. 5e and f. According to Fig. 5e, the HEO-P anode exhibits impressive rate capability, delivering substantial de-lithiation capacities at various C-rates, including 964, 459, 366, 284, and 181 mA h g^{-1} at C/10, C/5, C/3, C/2, and 1C, respectively. Upon resetting the C-rate from 1C to C/5, the capacity reverts to 328 mA h g^{-1}, indicating the stability of the HEO-P anode structure and its ability to accommodate significant changes in current density. Conversely, HEO demonstrates discharge capacities of 827, 174, 150, 110 and 45 mA h g^{-1} at C-rates of C/10, C/5, C/3, C/2 and 1C, respectively. The capacity decline is attributed to kinetic restrictions imposed by diffusion-driven processes during de-lithiation/lithiation reactions.

These findings suggest that HEO-P is a promising anode material for rate performance, which can be attributed to its stable structure and enhanced conductivity facilitated by the presence of PANI. In contrast to conversion-type anodes, the enhanced cycling stability of HEO electrodes is due to entropy stabilization effects that protect the HEO structure during lithiation and enhance the recovery of the spinel phase during delithiation, thereby ensuring the redox durability of the anode. The remarkable rate capability of HEO-P can be attributed to the enhanced electrical conductivity, which arises from the abundance of oxygen vacancies and enables improved charge transfer and storage properties of HEO [50].

Furthermore, the presence of abundant oxygen vacancies, as demonstrated in high-entropy oxides like $(CoNiZnFeMnLi)_3O_4$, significantly contributes to the enhanced rate performance and stability by providing additional active sites for lithium-ion storage and facilitating faster ion diffusion. This is consistent with how the PANI coating in our study serves as a mediator during the charging and discharging processes, minimizing volume changes caused by Li^+ transport and enhancing the electrochemical stability of the HEO material [32,51]. On the other hand, these findings are similar to the performance results of Sb_2MoO_6 @PANI synthesized by Yang et al., as an anode material for sodium-ion batteries [47].

Table 2 lists the electrochemical experimental results of the spinel-structured HEO in this study compared with those of other spinel-structured HEOs when used as LIB anode materials, which demonstrates that the novel spinel-structured HEO, as synthesized in this study, exhibits potential for lithium storage capabilities in lithium-ion batteries.

Electrochemical impedance spectroscopy (EIS) was used to measure the diffusion coefficient of lithium ions in the electrodes. EIS is a valuable analytical technique for understanding the reaction kinetics of the Li-ion insertion/deinsertion process in compounds, as it is non-destructive and capable of distinguishing between different phenomena occurring in an electrode over various time periods. To assess the electrical conductivity and Li^+ transfer in the HEO and HEO-P anodes, EIS plots before cycling were examined. The Nyquist plots in Fig. 6a exhibit a semicircle in the high-to-middle-frequency region, which represents the charge transfer resistance, ohmic resistance and SEI film resistance, and an oblique line in the low frequency region (representing Li^+ diffusion resistance). It is observed that the semicircle diameter of the HEO is larger than that of the HEO-P electrode, demonstrating lower charge-transfer resistance in HEO-P (~226 Ω) compared to HEO (~366 Ω). The semicircle diameter has a direct correlation with the impedance. The impedance data of all samples were analyzed by fitting equivalent circuits shown in Fig. 6, which include ohmic resistance (R_S), charge transfer resistance (R_{ct}), a constant-phase element (CPE), and Warburg impedance (Z_W). The Li-ion diffusion coefficient (D_{Li}^+) can be determined from EIS data using the following equation [58]:

$$D_{Li^+} = \frac{R^2T^2}{2A^2n^4F^4C^2\sigma_w^2} \quad (2)$$

The gas constant (R), Faraday constant (F), active surface area of the electrode (A), test temperature (T), number of electrons in the redox reaction (n), and concentration of lithium ions in the electrolyte (C) are denoted by these respective variables. The relationship between the real resistance (Z′) and the inverse square root of frequency ($\omega^{-1/2}$) of both the HEO and HEO-P electrodes is illustrated in Fig. 6b. The Warburg coefficient σ_w is related to Z′ through the expression:

$$Z' = R_s + R_{ct} + \sigma_w\omega^{-1/2} \quad (3)$$

In Fig. 6b, shows a linear correlation between Ź and $\omega^{-1/2}$. According to Eq. (3), σ_w represents the slope of the Z′-$\omega^{-1/2}$ curve. By linearly fitting the Z′-$\omega^{-1/2}$ curve, the σ_w values for HEO and HEO-P are determined as 267.73 and 204.95, respectively. Using Eq. (2), one can calculate the ratio of D_{Li+} (HEO-P) to D_{Li+} (HEO) by applying the given equation:

$$\frac{D_{Li^+}\ (\text{HEO-P})}{D_{Li^+}\ (\text{HEO})} = \frac{\sigma_w^2\ (\text{HEO})}{\sigma_w^2\ (\text{HEO-P})} \quad (4)$$

As a result, the lithium-ion diffusion coefficient of HEO-P is approximately 1.7 times higher than that of HEO, indicating the enhanced lithium-ion diffusion rate in PANI-modified HEO sample. The larger diffusion coefficient of lithium ions within the electrode material indicates that the kinetics of lithium ions transport can meet the reaction requirements at high charge/discharge currents, resulting in improved rate performance. This improved diffusion rate is attributable to the conductive PANI layer, which significantly enhances the surface conductivity of HEO, facilitating electron and ion transport. The presence of this conductive layer has substantial positive implications for the intercalation of lithium ions from the surface, thereby reducing the diffusion resistance of Li^+ in the solid phase.

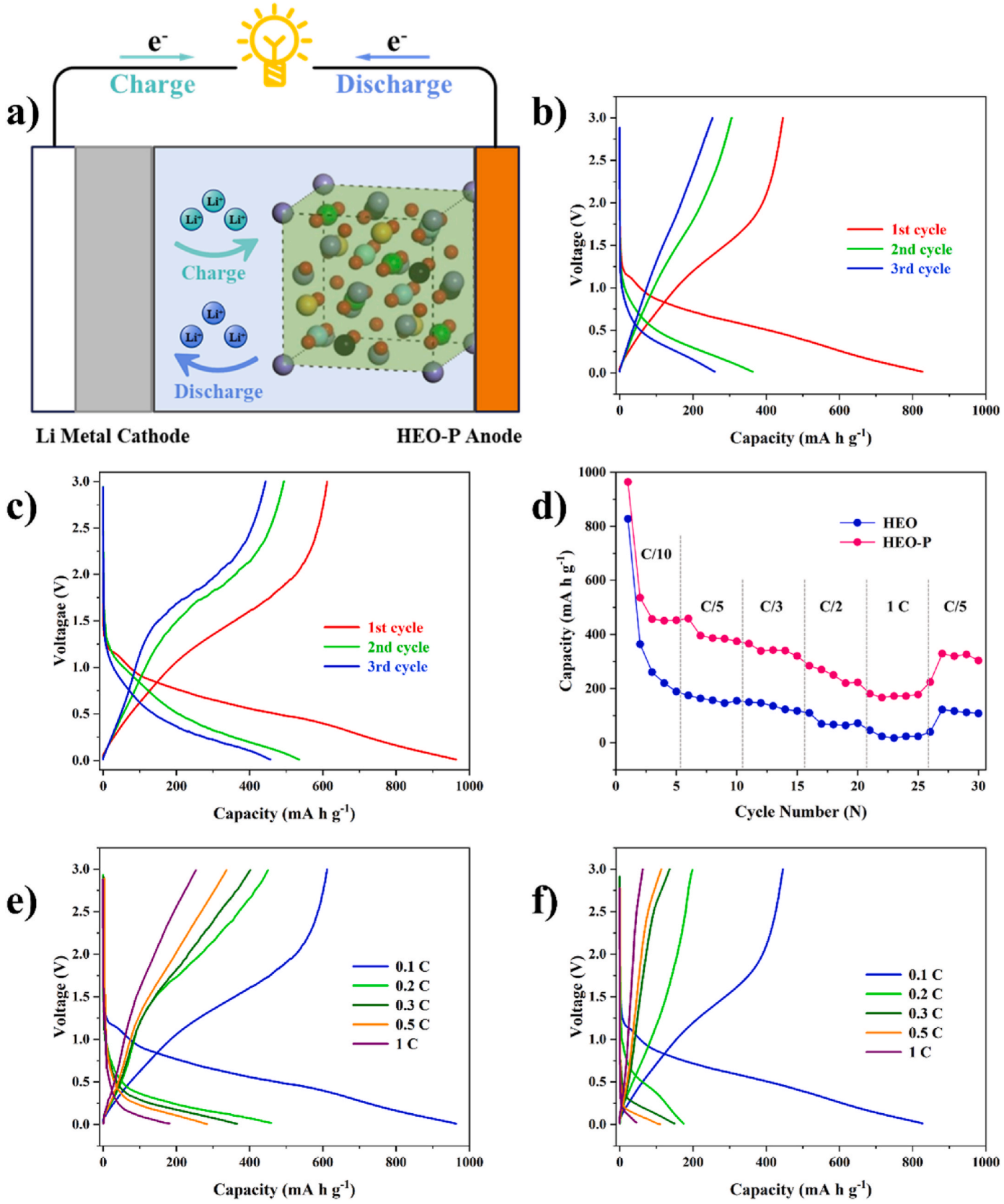

Fig. 5. (a) Schematic of half-cell, (b) HEO and (c)HEO-P charge/discharge voltage profiles for the first 3 cycles at C/10, (d) The rate capability of the HEO-P and HEO electrodes and (e, f) the corresponding galvanostatic charge-discharge curves of HEO-P and HEO electrodes, respectively.

Table 2
Synthesis methods and electrochemical properties of HEOs.

Materials	Method	Specific Capacity (Discharge/Charge) (mA h/g)	Rate Capability (mA h/g)	Ref.
Polyaniline-Modified $(FeCoNiCrMn)_3O_4$	Solid-state reaction	964/612 @ 200 mA g^{-1}	181 @ 2 A g^{-1}	This study
$)CrMnCoNiZn)_3O_4$	Sol–gel	1388/563 @ 100 mA g^{-1}	96 @ 2 A g^{-1}	[52]
$(MgTiZnNiFe)_3O_4$	Solid-state reaction	424.7/166.8 @ 100 mA g^{-1}	93.6 @ 1 A g^{-1}	[53]
$(MgTiZnCuFe)_3O_4$	Solid-state reaction	1261/634 @ 100 mA g^{-1}	268 @ 2 A g^{-1}	[54]
$(MnFeCoZnNi)_3O_4$	Electrospinning	1283.6/885.2 @ 20 mA g^{-1}	58 @ 2 A g^{-1}	[55]
$(CoTiZnNiFe)_3O_4$	Solid-state reaction	674.7/423.9 @ 100 mA g^{-1}	150.3 @ 1 A g^{-1}	[53]
(NiCoZnFeMg)O	Solid-state synthesis	820/575 @ 50 mA g^{-1}	304 @ 0.5 A g^{-1}	[56]
(MgCoNiCuZn)O	Solid-state synthesis	1585/976 @ 100 mA g^{-1}	490 @ 3 A g^{-1}	[57]

The HEO-P electrode shows excellent capacity retention and high rate capability compared to the HEO electrode, which is attributed to the formation of a stable SEI layer. This SEI layer maintains its structural integrity during repeated cycling, ensuring the electrode's long-term stability. To confirm this, the FE-SEM of the cycled electrode was conducted to further explore the protective effect of the PANI coating. The images of HEO and HEO-P anodes before and after 30 cycles are shown in Fig. 7. In contrast, a non-uniform SEI layer is formed on the HEO electrode after 30 cycles, resulting in multiple cracks (Fig. 7b and c). However, a smooth and compact surface is observed for the HEO-P electrode after 30 cycles (Fig. 7e and f). Despite high magnification, hardly any severe cracking or fracture was observed on the HEO-P electrode, indicating the formation of a stable SEI layer. This stability is a testament to the electrode's ability to accommodate large volume changes during lithiation/de-lithiation reactions and form a stable SEI layer. Consequently, the HEO-P electrode exhibits excellent cycling stability and high rate capability, which are crucial attributes for an anode in Li-ion batteries. In contrast, the HEO electrode exhibits severe cracking after 30 cycles, and its original spherical morphology is no longer maintained. This suggests that the HEO is unable to buffer large volume changes during the conversion reaction and breaks down during repeated cycling, leading to the exposure of fresh HEO surface to electrolyte and continued SEI formation. As a result, this can lead to capacity fading and poor coulombic efficiencies. However, the HEO-P electrode, which features a protective PANI coating, maintains a stable SEI layer. This layer appears to be effective in preventing agglomeration, pulverization, and volume changes of HEO during lithiation/de-lithiation reactions, thereby avoiding SEI cracking, the formation of non-conductive impurities, and maintains electrode integrity, thereby enhancing the rate of mass transfer capability and improving the overall performance of the electrodes, thereby enhancing both the rate of mass transfer and conductivity capability of the electrodes, thereby enhancing the overall capability of the electrodes. To sum up, the enhanced electrochemical performance of HEO-P is attributed to the uniform PANI coating layer, which overcomes the limitations of HEOs, including their poor conductivities and susceptibility to fracture during volume expansion. The conductive PANI, with its conjugated π electron system, significantly enhances the conductivity of HEO, serving not only as a conductive pathway but also as a protective barrier that shields the HEO surface from in-service degradation. Furthermore, the highly conductive PANI coating, surrounding each HEO particles, facilitates efficient lithium ion transfer within the electrode, thereby enhancing the overall performance of the electrodes.

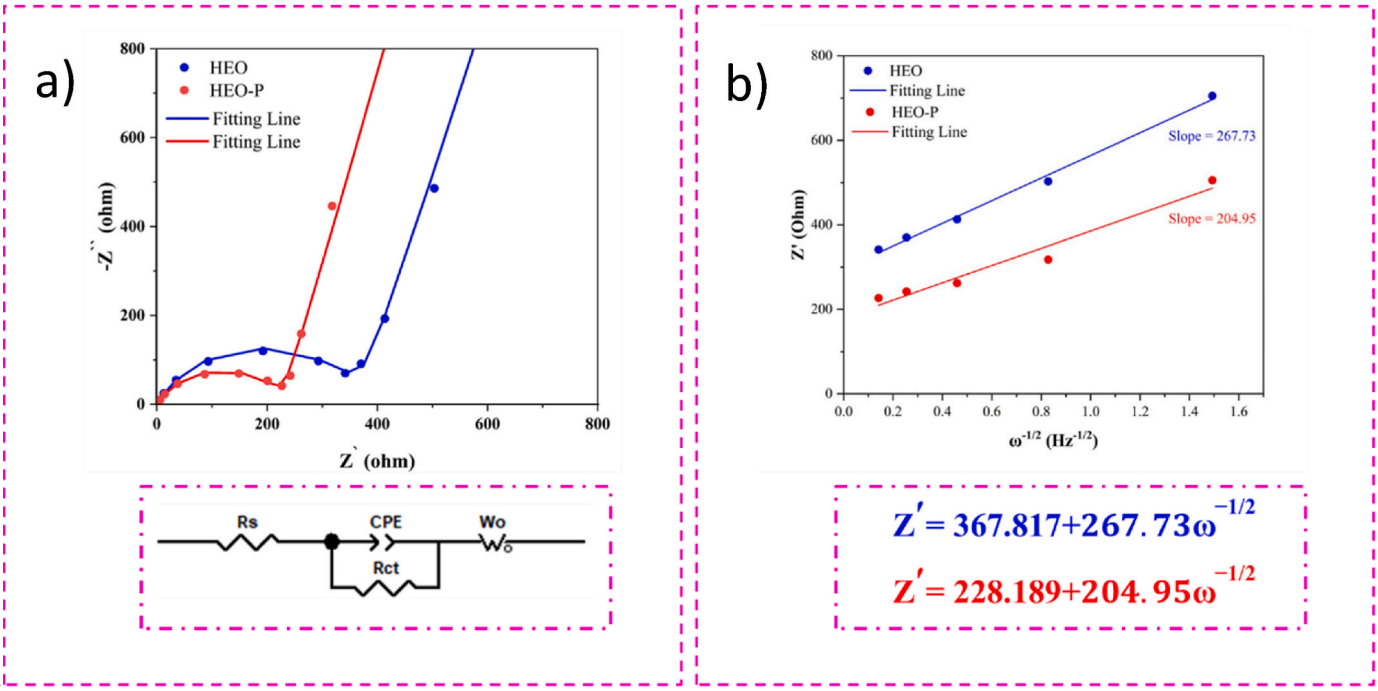

Fig. 6. (a) Nyquist plots of HEO (blue) and HEO-P (red) electrodes and (b) their plots of Warburg resistance as a function of inverse square root of angular frequency. (For interpretation of the references to colour in this figure legend, the reader is referred to the Web version of this article.)

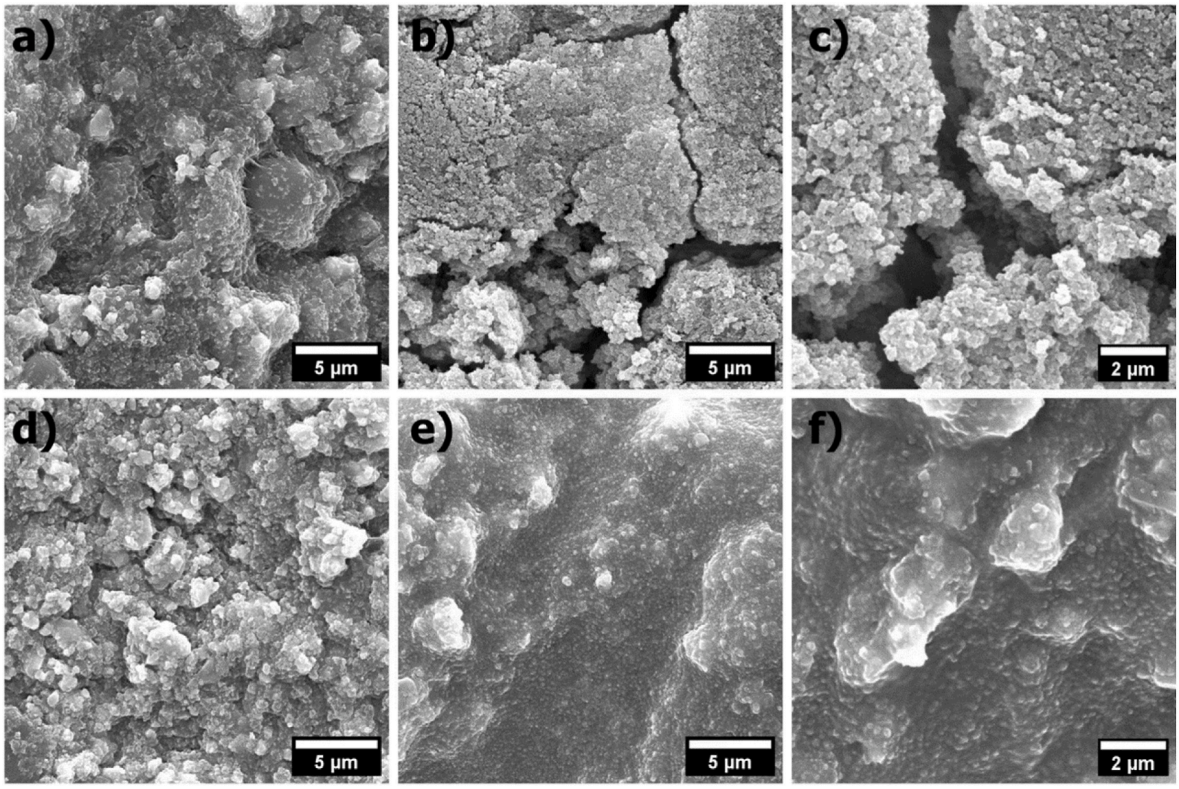

Fig. 7. FESEM images of a) HEO anode before cycling, b, c) after cycling; d) HEO-P anode before cycling (e, f) after cycling.

4. Conclusions

In summary, a high entropy oxide $(FeCoNiCrMn)_3O_4$ with a spinel structure was synthesized via a solid state reaction. Then, a Polyaniline (PANI) coating layer was deposited onto the HEO particles using a polymerization method. The PANI-modified powder samples were utilized as anode material for Li-ion batteries. XRD results showed a structural transformation during milling, resulting in the formation of the spinel structure with multi-element transition metal oxides. Calcination at 900 °C led to the formation of a single-phase pure spinel HEO. The HEO anode showed high specific discharge capacity, attributed to its optimal electron configurations, facile ion diffusion pathways, and abundant active storage sites derived from its unique mixed-valence structure, comprising diverse cation radii and multiple metal elements. The results showed that in HEO-P, the PANI coating layer in HEO-P significantly enhanced the electrochemical performance of the anode material by improving its structural stability and inhibiting excessive SEI growth during cycling. Moreover, the PANI coating significantly improves the reactions between electrodes and electrolyte. Upon testing, HEO-P exhibits a high reversible capacity of 964 mA h g^{-1} at C-rate of C/10 and excellent rate capability performance of 104 mA h g^{-1} at C-rate of 1 C. The PANI-modified HEO appears to be a promising candidate for use as an electrode material in advanced Li-ion batteries.

CRediT authorship contribution statement

Arezoo Jari: Writing – original draft, Methodology, Investigation, Data curation, Conceptualization. **Masoud Panjepour:** Writing – review & editing, Supervision, Methodology, Investigation, Conceptualization. **Abbas Bahrami:** Writing – review & editing, Validation, Supervision, Resources, Formal analysis. **Maryam Yazdan Mehr:** Writing – review & editing, Validation, Supervision, Methodology, Investigation, Formal analysis.

Declaration of competing interest

The authors declare that they have no known competing financial interests or personal relationships that could have appeared to influence the work reported in this paper.

Data availability

Data will be made available on request.

References

[1] P. Luo, Z. Huang, T. Wang, H. Xiao, X. Ma, R. Yan, G. Zhao, Design and fabrication of nitrogen-doped graphene-promoted Na3MnTi(PO4)3@C cathode with three-electron reactions for sodium-ion storage, Solid State Sci. 156 (2024) 107678.
[2] L. Zhou, S. Li, A. Jain, G. Chen, D. Guo, J. Kang, Y. Zhao, Lithium battery thermal management based on lightweight stepped-channel liquid cooling, J. Electrochem. Energy Conv. Storage 21 (3) (2024) 031012.
[3] W. Huang, Y. Sun, G. Zhao, Q. Liu, G. Zhao, L. Duan, Q. An, F. Ren, M. Sun, S. Xia, H. Guo, Constructing nano spinel phase and Li+ conductive network to enhance the electrochemical stability of ultrahigh-Ni cathode, Mater. Today 79 (2024) 86–96.
[4] V. Etacheri, R. Marom, R. Elazari, G. Salitra, D. Aurbach, Challenges in the development of advanced Li-ion batteries: a review, Energy Environ. Sci. 4 (2011) 3243–3262.
[5] P.G. Bruce, B. Scrosati, J. Tarascon, Nanomaterials for rechargeable lithium batteries, Angew. Chem. Int. Ed. 47 (2008) 2930–2946.
[6] T. Ould Ely, D. Kamzabek, D. Chakraborty, Batteries safety: recent progress and current challenges, Front. Energy Res. 7 (2019) 71.
[7] H. Zhang, Y. Yang, D. Ren, L. Wang, X. He, Graphite as anode materials: fundamental mechanism, recent progress and advances, Energy Storage Mater. 36 (2021) 147–170.
[8] S. Lim, J.-H. Kim, Y. Yamada, H. Munakata, Y.-S. Lee, S.-S. Kim, K. Kanamura, Improvement of rate capability by graphite foam anode for Li secondary batteries, J. Power Sources 355 (2017) 164–170.
[9] S. Menkin, Z. Barkay, D. Golodnitsky, E. Peled, Nanotin alloys supported by multiwall carbon nanotubes as high-capacity and safer anode materials for EV lithium batteries, J. Power Sources 245 (2014) 345–351.
[10] H. Zhao, J. Li, Q. Zhao, X. Huang, S. Jia, J. Ma, Y. Ren, Si-based anodes: advances and challenges in Li-ion batteries for enhanced stability, Electrochem. Energy Rev. 7 (2024) 11.

[11] C. Ding, S. Li, X. Zeng, W. Wang, M. Wang, T. Liu, C. Liang, Precise construction of Sn/C composite membrane with graphene-like Sn-in-Carbon structural units toward hyperstable anode for lithium storage, ACS Appl. Mater. Interfaces 15 (2023) 12189–12201.

[12] Y. Zhao, X. Li, B. Yan, D. Xiong, D. Li, S. Lawes, X. Sun, Recent developments and understanding of novel mixed transition-metal oxides as anodes in lithium ion batteries, Adv. Energy Mater. 6 (2016) 1502175.

[13] S. Fang, D. Bresser, S. Passerini, Transition metal oxide anodes for electrochemical energy storage in lithium-and sodium-ion batteries, Transit. Met. Oxides Electrochem. Energy Storage (2022) 55–99.

[14] X. Yang, H. Wang, Y. Song, K. Liu, T. Huang, X. Wang, C. Zhang, J. Li, Low-temperature synthesis of a porous high-entropy transition-metal oxide as an anode for high-performance lithium-ion batteries, ACS Appl. Mater. Interfaces 14 (13) (2022).

[15] C. Liang, M. Gao, H. Pan, Y. Liu, M. Yan, Lithium alloys and metal oxides as high-capacity anode materials for lithium-ion batteries, J. Alloys Compd. 575 (2013) 246–256.

[16] A. Casimir, H. Zhang, O. Ogoke, J.C. Amine, J. Lu, G. Wu, Silicon-based anodes for lithium-ion batteries: effectiveness of materials synthesis and electrode preparation, Nano Energy 27 (2016) 359–376.

[17] C. Gao, J. Zhu, S. Ye, M. Li, H. Wang, J. He, Novel high-entropy perovskite titanate: a potential thermal protective material with improved thermophysical properties, J. Eur. Ceram. Soc. 45 (2) (2025) 116878.

[18] Y.X. Yu, J.L. Xu, L.W. Zhang, Y.C. Ma, J.M. Luo, Electrochemically treated AlCoCrFeNi high entropy alloy as a self-supporting electrode for overall water splitting, Int. J. Hydrogen Energy 72 (2024) 209–219.

[19] A. Fu, Z. Xie, J. Wang, Y. Cao, B. Wang, J. Li, Q. Fang, X. Li, B. Liu, Y. Liu, Controlling of cellular substructure and its effect on mechanical properties of FeCoCrNiMo0.2 high entropy alloy fabricated by selective laser melting, Mater. Sci. Eng., A 901 (2024) 146547.

[20] A. Sarkar, Q. Wang, A. Schiele, M.R. Chellali, S.S. Bhattacharya, D. Wang, T. Brezesinski, H. Hahn, L. Velasco, B. Breitung, High-entropy oxides: fundamental aspects and electrochemical properties, Adv. Mater. 31 (2019) 1806236.

[21] C.M. Rost, E. Sachet, T. Borman, A. Moballegh, E.C. Dickey, D. Hou, J.L. Jones, S. Curtarolo, J.-P. Maria, Entropy-stabilized oxides, Nat. Commun. 6 (2015) 1–8.

[22] A. Sarkar, L. Velasco, D. Wang, Q. Wang, G. Talasila, L.D. Biasi, T. Brezesinski, S. S. Bhattacharya, H. Hahn, B. Breitung, High entropy oxides for reversible energy storage, Nat 24 (9) (2018) 3400.

[23] K. Tian, H. He, X. Li, D. Wang, Z. Wang, R. Zheng, H. Sun, Y. Liu, Q. Wang, Boosting electrochemical reaction and suppressing phase transition with a high-entropy O3-type layered oxide for sodium-ion batteries, J. Mater. Chem. A 10 (2022) 14943–14953.

[24] N. Qiu, H. Chen, Z. Yang, S. Sun, Y. Wang, Y. Cui, A high entropy oxide (Mg0. 2Co0. 2Ni0. 2Cu0. 2Zn0. 2O) with superior lithium storage performance, J. Alloys Compd. 777 (2019) 767–774.

[25] D. Bérardan, S. Franger, A.K. Meena, N. Dragoe, Room temperature lithium superionic conductivity in high entropy oxides, J. Mater. Chem. A 4 (2016) 9536–9541.

[26] J.-W. Yeh, S.-J. Lin, Breakthrough applications of high-entropy materials, J. Mater. Res. 33 (2018) 3129–3137.

[27] D. Wang, Z. Liu, S. Du, Y. Zhang, H. Li, Z. Xiao, W. Chen, R. Chen, Y. Wang, Y. Zou, Low-temperature synthesis of small-sized high-entropy oxides for water oxidation, J. Mater. Chem. A 7 (2019) 24211–24216.

[28] M. Stygar, J. Dąbrowa, M. Moździerz, M. Zajusz, W. Skubida, K. Mroczka, K. Berent, K. Świerczek, M. Danielewski, Low-temperature synthesis of small-sized high-entropy oxides for water oxidation, J. Eur. Ceram. Soc. 40 (2020) 1644–1650.

[29] Z. Grzesik, G. Smoła, M. Miszczak, M. Stygar, J. Dąbrowa, M. Zajusz, K. Świerczek, M. Danielewski, Defect structure and transport properties of (Co, Cr, Fe, Mn, Ni) 3O4 spinel-structured high entropy oxide, J. Eur. Ceram. Soc. 40 (2020) 835–839.

[30] T.X. Nguyen, J. Patra, J.-K. Chang, J.-M. Ting, High entropy spinel oxide nanoparticles for superior lithiation–delithiation performance, J. Mater. Chem. A 8 (2020) 18963–18973.

[31] D. Wang, S. Jiang, C. Duan, J. Mao, Y. Dong, K. Dong, Z. Wang, S. Luo, Y. Liu, X. Qi, Spinel-structured high entropy oxide (FeCoNiCrMn) 3O4 as anode towards superior lithium storage performance, J. Alloys Compd. 844 (2020) 156158.

[32] K.-H. Tian, C.-Q. Duan, Q. Ma, X.-L. Li, Z.-Y. Wang, H.-Y. Sun, S.-H. Luo, D. Wang, Y.-G. Liu, High-entropy chemistry stabilizing spinel oxide (CoNiZnXMnLi) 3O4 (X= Fe, Cr) for high-performance anode of Li-ion batteries, Rare Met. 41 (2022) 1265–1275.

[33] Y. Zheng, X. Wu, X. Lan, R. Hu, A spinel (FeNiCrMnMgAl) 3O4 high entropy oxide as a cycling stable anode material for Li-ion batteries, Processes 10 (2021) 49.

[34] J. Dąbrowa, M. Stygar, A. Mikuła, A. Knapik, K. Mroczka, W. Tejchman, M. Danielewski, M. Martin, Synthesis and microstructure of the (Co, Cr, Fe, Mn, Ni) 3O4 high entropy oxide characterized by spinel structure, Mater. Lett. 216 (2018) 32–36.

[35] W. Wang, Y. Wang, L. Yuan, C. You, J. Wu, L. Liu, J. Ye, Y. Wu, L. Fu, Recent advances in modification strategies of silicon-based lithium-ion batteries, Nano Res. 16 (2023) 3781–3803.

[36] Y. Zeng, Y. Huang, N. Liu, X. Wang, Y. Zhang, Y. Guo, H.-H. Wu, H. Chen, X. Tang, Q. Zhang, N-doped porous carbon nanofibers sheathed pumpkin-like Si/C composites as free-standing anodes for lithium-ion batteries, J. Energy Chem. 54 (2021) 727–735.

[37] Z. Huang, P. Luo, H. Zheng, Z. Lyu, X. Ma, Novel one-dimensional V3S4@ NC nanofibers for sodium-ion batteries, J. Phys. Chem. Solid. 172 (2023) 111081.

[38] N. Shin, M. Kim, J. Ha, Y.-T. Kim, J. Choi, Flexible anodic SnO2 nanoporous structures uniformly coated with polyaniline as a binder-free anode for lithium ion batteries, J. Electroanal. Chem. 914 (2022) 116296.

[39] H. Wiggers, Y.H. Sehlleier, F. Kunze, L. Xiao, S.M. Schnurre, C. Schulz, Self-assembled nano-silicon/graphite hybrid embedded in a conductive polyaniline matrix for the performance enhancement of industrial applicable lithium-ion battery anodes, Solid State Ionics 344 (2020) 115117.

[40] C. Zhang, Q. Chen, X. Ai, X. Li, Q. Xie, Y. Cheng, H. Kong, W. Xu, L. Wang, M.-S. Wang, spine, J. Mater. Chem. A 8 (2020) 16323–16331.

[41] W. Zhang, P.K. Liaw, Y. Zhang, Science and technology in high-entropy alloys, Sci. China Mater. 61 (2018) 2–22.

[42] S.S. Aamlid, M. Oudah, J. Rottler, A.M. Hallas, Understanding the role of entropy in high entropy oxides, J. Am. Chem. Soc. 145 (2023) 5991–6006.

[43] A. Sarkar, B. Breitung, H. Hahn, High entropy oxides: the role of entropy, enthalpy and synergy, Scripta Mater. 187 (2020) 43–48.

[44] Advanced Materials - 2019 - Sarkar - High-Entropy Oxides Fundamental Aspects and Electrochemical Properties.Pdf, (n.d.).

[45] S. Pourmohammadi, A. Mohammadnejad, A. Bahrami, S.H. Mousavi Anijdan, N. Park, M. Ghosh, Phase stability, microstructure, and mechanical properties of spark plasma sintered nanocrystalline boron-doped AlCoFeMnNi high-entropy alloy, Metals 13 (6) (2023) 1025.

[46] A. Bahrami, A. Mohammadnejad, M. Sajadi, Microstructure and mechanical properties of spark plasma sintered AlCoFeMnNi high entropy alloy (HEA)-Carbon nanotube (CNT) nanocomposite, J. Alloys Compd. 862 (5) (2021) 158577.

[47] L. Yang, H. Liao, Y. Tian, W. Hong, P. Cai, C. Liu, Y. Yang, G. Zou, H. Hou, X. Ji, Rod-like Sb2MoO6: structure evolution and sodium storage for sodium-ion batteries, Small Methods 3 (2019) 1800533.

[48] T. Zheng, G. Li, L. Zhao, Y. Shen, Flowerlike Sb2S3/PPy microspheres used as anode material for high-performance sofile:///D:/battery project/high entropy/2-for my experimental work/MgCoNiCuZn.pdfdium-Ion batteries, Eur. J. Inorg. Chem. 2018 (2018) 1224–1228.

[49] Y. Wang, W. Wu, L. Cheng, P. He, C. Wang, Y. Xia, A polyaniline-intercalated layered manganese oxide nanocomposite prepared by an inorganic/organic interface reaction and its high electrochemical performance for Li storage, Adv. Mater. 20 (2008) 2166–2170.

[50] Y. Gu, A. Bao, X. Wang, Y. Chen, L. Dong, X. Liu, H. Pan, Y. Li, X. Qi, Engineering the oxygen vacancies of rocksalt-type high-entropy oxides for enhanced electrocatalysis, Nanoscale 14 (2022) 515–524.

[51] L. Zhou, S. Li, A. Jain, G. Sun, G. Chen, D. Guo, J. Kang, Y. Zhao, Optimization of thermal non-uniformity challenges in liquid-cooled lithium-ion battery packs using NSGA-II, J. Electrochem. Energy Conv. Storage 22 (4) (2025) 041002.

[52] C. Jin, Y. Wang, H. Dong, Y. Wei, R. Nan, Z. Jian, Z. Yang, Q. Ding, A novel spinel high-entropy oxide (Cr0. 2Mn0. 2Co0. 2Ni0. 2Zn0. 2) 3O4 as anode material for lithium-ion batteries, INORGA 12 (2024) 198.

[53] C. Liu, J. Bi, L. Xie, X. Gao, L. Meng, Preparation and electrochemical properties of two novel high entropy spinel oxides (MgTiZnNiFe) 3O4 and (CoTiZnNiFe) 3O4 by solid state reaction, Mater. Today Commun. 35 (2023) 106315.

[54] H. Chen, N. Qiu, B. Wu, Z. Yang, S. Sun, Y. Wang, A new spinel high-entropy oxide (Mg 0.2 Ti 0.2 Zn 0.2 Cu 0.2 Fe 0.2) 3 O 4 with fast reaction kinetics and excellent stability as an anode material for lithium ion batteries, RSC Adv. 10 (2020) 9736–9744.

[55] C. Triolo, M. Maisuradze, M. Li, Y. Liu, A. Ponti, G. Pagot, V. Di Noto, G. Aquilanti, N. Pinna, M. Giorgetti, Charge storage mechanism in electrospun spinel-structured high-entropy (Mn0. 2Fe0. 2Co0. 2Ni0. 2Zn0. 2) 3O4 oxide nanofibers as anode material for Li-ion batteries, Small 19 (2023) 2304585.

[56] O.J.B.J. Marques, M.D. Walter, E.V. Timofeeva, C.U. Segre, Effect of initial structure on performance of high-entropy oxide anodes for li-ion batteries, Batteries 9 (2023) 115.

[57] N. Qiu, H. Chen, Z. Yang, S. Sun, Y. Wang, Y. Cui, A high entropy oxide (Mg0.2Co0.2Ni0.2Cu0.2Zn0.2O) with superior lithium storage performance, J. Alloys Compd. 777 (2019) 767–774, https://doi.org/10.1016/j.jallcom.2018.11.049.

[58] H. Shu, X. Wang, Q. Wu, L. Liu, Q. Liang, S. Yang, B. Ju, X. Yang, X. Zhang, Y. Wang, The effect of ammonia concentration on the morphology and electrochemical properties of LiFePO4 synthesized by ammonia assisted hydrothermal route, Electrochim. Acta 76 (2012) 120–129.